Class. Quantum Grav. **25** (2008) 205007 (20pp) doi:10.1088/0264-9381/25/20/205007

First joint gravitational wave search by the AURIGA–EXPLORER–NAUTILUS–Virgo Collaboration

F Acernese[ac,1], M Alshourbagy[ab,2], P Amico[ab,3], F Antonucci[a,4], S Aoudia[5], P Astone[a,4], S Avino[ab,1], D Babusci[6], L Baggio[7,31], G Ballardin[8], F Barone[ac,1], L Barsotti[ab,2], M Barsuglia[9], M Bassan[ab,10], Th S Bauer[a,11], M Bignotto[12,13], S Bigotta[ab,2], S Birindelli[ab,2], M A Bizouard[9], C Boccara[b,1], M Bonaldi[14,15], F Bondu[5], L Bosi[a,3], S Braccini[b,2], C Bradaschia[b,2], A Brillet[5], V Brisson[9], D Buskulic[7], G Cagnoli[a,16], E Calloni[ab,1], M Camarda[17], E Campagna[ac,16], F Carbognani[8], P Carelli[ac,10], F Cavalier[9], R Cavalieri[8], G Cavallari[18], G Cella[a,2], M Cerdonio[12,13], E Cesarini[ab,16], E Chassande-Mottin[5], A Chincarini[19], A-C Clapson[9], F Cleva[5], E Coccia[ab,10], L Conti[12,13], C Corda[ab,2], A Corsi[a,4], F Cottone[ab,3], J-P Coulon[5], E Cuoco[8], S D'Antonio[a,10], A Dari[ab,3], V Dattilo[8], M Davier[9], R De Rosa[ab,1], M Del Prete[ad,2], L Di Fiore[9], A Di Lieto[ab,2], M Di Paolo Emilio[ac,10], A Di Virgilio[a,2], M Drago[12,13], F Dubath[20], M Evans[8], V Fafone[ab,10], P Falferi[14,15], I Ferrante[ab,2], F Fidecaro[ab,2], I Fiori[8], R Flaminio[5], S Foffa[20], P Fortini[21,22], J-D Fournier[2], S Frasca[ab,4], F Frasconi[a,2], L Gammaitoni[ab,3], F Garufi[ab,1], G Gemme[19], E Genin[8], A Gennai[a,2], A Giazotto[8,a,2], G Giordano[6], L Giordano[ab,1], V Granata[7], C Greverie[5], D Grosjean[7], G Guidi[ac,16], S Hamdani[8], S Hebri[8], H Heitmann[5], P Hello[9], D Huet[8], S Kreckelbergh[9], P La Penna[8], M Laval[5], N Leroy[9], N Letendre[7], N Liguori[12,13], S Longo[23], B Lopez[8], M Lorenzini[ab,16], V Loriette[24], G Losurdo[a,16], J-M Mackowski[25], M Maggiore[20], E Majorana[a,4], C N Man[5], M Mantovani[bd,2], F Marchesoni[ab,3], A Marini[6], F Marion[7], J Marque[8], F Martelli[ac,16], A Masserot[7], F Menzinger[8], R Mezzena[15,26], L Milano[ab,1], Y Minenkov[a,10], A Mion[15,26], I Modena[ab,10], G Modestino[6], C Moins[8], A Moleti[ab,10], J Moreau[24], N Morgado[25], S Mosca[ab,1], B Mours[7], I Neri[ab,3], F Nocera[8], A Ortolan[23], G Pagliaroli[a,10], G V Pallottino[ab,4], C Palomba[a,4], F Paoletti[8,a,2], S Pardi[ab,1], R Parodi[19], A Pasqualetti[8], R Passaquieti[ab,2], D Passuello[a,2], G Piano Mortari[c,10,27], F Piergiovanni[ac,16], L Pinard[25], G Pizzella[bc,10], S Poggi[28], R Poggiani[ab,2], G A Prodi[15,26], M Punturo[a,3], P Puppo[a,4], L Quintieri[6], P Rapagnani[ab,4], V Re[15,26], T Regimbau[5], A Remillieux[25], F Ricci[ab,4], I Ricciardi[ab,1], A Rocchi[a,10], L Rolland[7], R Romano[ac,1], F Ronga[6], P Ruggi[8], G Russo[ab,1], F Salemi[15,26], S Solimeno[ab,1], A Spallicci[5], R Sturani[20], L Taffarello[13], M Tarallo[ab,2], R Terenzi[a,10], A Toncelli[ab,2], M Tonelli[ab,2], G Torrioli[a,4,29], E Tournefier[7], F Travasso[ab,3], C Tremola[ab,2], R Vaccarone[19], G Vajente[bc,2],

[31] Presently at Centre d'Etudes des Environnements Terrestre et Plantaires (CETP), 10-12 Avenue de l'Europe, 78140 Velizy, France.

0264-9381/08/205007+20$30.00

G Vandoni[18], G Vedovato[12], J F J van der Brand[ab,11], S van der Putten[ab,11], D Verkindt[7], F Vetrano[ac,16], A Viceré[ac,16], A Vinante[14,15], J-Y Vinet[5], M Visco[a,10,30], S Vitale[15,26], H Vocca[a,3], M Yvert[7] and J P Zendri[13]

[1] INFN, Sezione di Napoli [a]; Università di Napoli 'Federico II' Complesso Universitario di Monte S Angelo[b], Napoli; Università di Salerno, Fisciano (Sa)[c], Italy
[2] INFN, Sezione di Pisa[a]; Università di Pisa[b]; Scuola Normale Superiore, Pisa[c]; Università di Siena, Siena[d], Italy
[3] INFN, Sezione di Perugia[a]; Università di Perugia, Perugia, Italy[b]
[4] INFN, Sezione di Roma[a]; Università 'La Sapienza'[b], Roma, Italy
[5] Artemis, Observatoire de la Côte d'Azur, CNRS, BP 4229 06304 Nice, Cedex 4, France
[6] INFN, Laboratori Nazionali di Frascati, Frascati, Italy
[7] Laboratoire d'Annecy-le-Vieux de Physique des Particules (LAPP), IN2P3/CNRS, Université de Savoie, Annecy-le-Vieux, France
[8] European Gravitational Observatory (EGO), Cascina (Pi), Italy
[9] LAL, Université Paris-Sud, IN2P3/CNRS, Orsay, France
[10] INFN, Sezione di Roma Tor Vergata[a]; Università di Roma Tor Vergata, Roma[b]; Università dell'Aquila, L'Aquila[c], Italy
[11] National institute for subatomic physics, NL-1009 DB[a]; Vrije Universiteit, NL-1081 HV [b], Amsterdam, The Netherlands
[12] Dipartimento di Fisica, Università di Padova, Via Marzolo 8, 35131 Padova, Italy
[13] INFN, Sezione di Padova, Via Marzolo 8, 35131 Padova, Italy
[14] Istituto di Fotonica e Nanotecnologie, CNR-Fondazione Bruno Kessler, I-38050 Povo (Trento), Italy
[15] INFN, Gruppo Collegato di Trento, Sezione di Padova, I-38050 Povo, Trento, Italy
[16] INFN, Sezione di Firenze, Sesto Fiorentino[a]; Università degli Studi di Firenze[b], Firenze; Università degli Studi di Urbino 'Carlo Bo', Urbino[c], Italy
[17] Dipartimento di Ingegneria Informatica, Università di Padova, Via G. Gradenigo 6a, 35131 Padova, Italy
[18] CERN, Geneva, Switzerland
[19] INFN, Sezione di Genova, Genova, Italy
[20] Dep. de Phys. Thèorique, Universitè de Genéve, Genéve, Switzerland
[21] Dipartimento di Fisica, Università di Ferrara, I-44100 Ferrara, Italy
[22] INFN, Sezione di Ferrara, I-44100 Ferrara, Italy
[23] INFN, Laboratori Nazionali di Legnaro, 35020 Legnaro, Padova, Italy
[24] ESPCI - 10, rue Vauquelin, 75005 Paris - France
[25] Laboratoire des Matériaux Avancés (LMA), IN2P3/CNRS, F-69622 Villeurbanne, Lyon, France
[26] Dipartimento di Fisica, Università di Trento, I-38050 Povo, Trento, Italy
[27] INFN, Laboratori Nazionali del Gran Sasso, Assergi, L'Aquila, Italy
[28] Consorzio Criospazio Ricerche, I-38050 Povo, Trento, Italy
[29] CNR, Istituto di Fotonica e Nanotecnologie, Roma, Italy
[30] INAF, Istituto Fisica Spazio Interplanetario, Roma, Italy

E-mail: lucio.baggio@lnl.infn.it, gianluca.guidi@uniurb.it and virginia.re@lnl.infn.it

Received 16 November 2007, in final form 30 June 2008
Published 30 September 2008
Online at stacks.iop.org/CQG/25/205007

Abstract

We present a methodology of network data analysis applied to the search for coincident burst excitations over a 24 h long data set collected by AURIGA, EXPLORER, NAUTILUS and Virgo detectors during September 2005. The search of candidate triggers was performed independently on each of the data sets from single detectors. We looked for two-fold time coincidences between these candidates using an algorithm optimized for a given population of sources

and we calculated the efficiency of detection through injections of templated signal waveforms into the streams of data. To this end we have considered the case of signals shaped as damped sinusoids coming from the galactic center direction. Our method targets an optimal balance between high efficiency and low false alarm rate, aiming at setting confidence intervals as stringent as possible in terms of the rate of the selected source models.

PACS numbers: 04.80.Nn, 95.55.Ym, 95.30.Sf, 95.85.Sz, 07.05.Kf

1. Introduction

The network composed by the three gravitational wave (GW) resonant detectors AURIGA [1, 2], EXPLORER and NAUTILUS [3, 4] and the interferometer Virgo [5] (hereafter called Virgo-bars network) is heterogeneous, as its single components differ for spectral sensitivity (see figure 1) and antenna pattern.

In the past few years, various searches for GW signals have been independently performed by individual detectors or by networks of resonant bars (IGEC [6, 7], ROG [8–10]) or interferometers [11–13]. In the latter cases the networks were homogeneous: almost same antenna pattern (neglecting a small misalignment), similar (within a factor of 2) integrated sensitivity and roughly the same observed frequency range (or detection bands). Therefore, a GW burst would produce approximately the same response in all the detectors of the network (notably, irrespective of the direction and polarization of the source). In such cases, the magnitude of observed signals can be compared directly.

Previous burst searches among detectors with different spectral sensitivity and orientation were performed by the TAMA and LIGO Scientific Collaboration [14] among interferometers and by the AURIGA and LIGO Scientific Collaborations [15, 16] between interferometers and a resonant bar.

Our aim in this paper is to develop and apply a new network search strategy which, following the line proposed in the IGEC coincidence search for burst GW signals, can result in a near optimal use of data coming from instruments of different sensitivity and antenna pattern. The IGEC search was innovative with respect to previous searches as it preserved the detection efficiency by selecting the detectors which, from time to time, had comparable directional sensitivity for sources located at a given sky position. In that case, however, there was no optimization on the detection efficiency and the analysis relied on identical antenna patterns for the detectors. Instead, for the Virgo-bars network, it is necessary to further develop the idea included in the IGEC strategy. The detection efficiency will be determined by studying the software injections (Mock Data Challenge, in the following referred to as MDC) of a given collection of target waveforms. The approach attempted in this work is to use the efficiency computation both to tune the analysis parameters and to calibrate the final results, a step missing in [7]. The coincident counts, divided by the detection efficiency and the observation time, then become observed rates (or upper limits on rates) for that particular source population.

In order to test the method, we performed an end-to-end analysis over a 24 h long data set collected by our network of detectors during September 2005, focusing on the two-fold coincidences between detectors: the aim is to maximize the common observation time and the detection efficiency of our heterogeneous network, thus resulting in better upper limits.

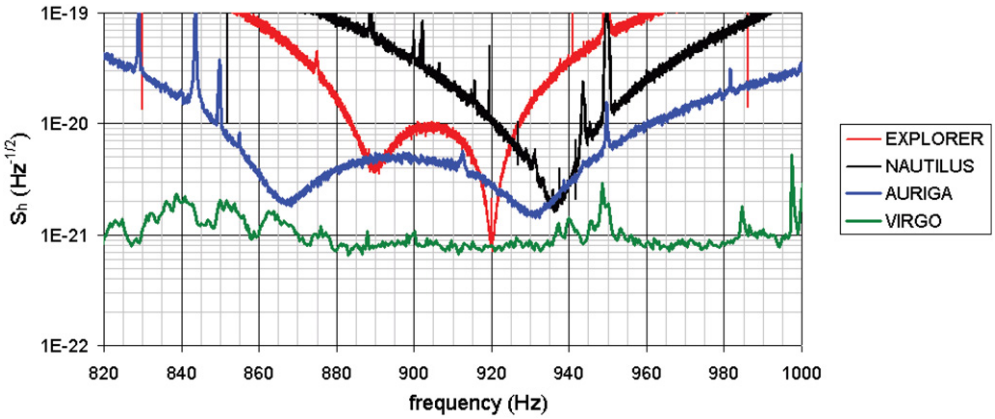

Figure 1. Typical spectral density of calibrated noise for the three resonant bar detectors during 2005 and for the Virgo interferometer in September 2005.

Nonetheless, the method is general and can be applied to n-fold coincidences. The results presented are obtained in the simpler case of fixed time coincidence windows.

The paper is organized as follows: we first describe, in section 2, the new coincident search strategy adopted in this work as well as the background and efficiency estimation procedure. Then we outline, in section 3, the actual implementation of our method to the 24 h of data exchanged by the collaborations. We thus introduce the target GW signals and the source population we are dealing with, give an overview of the exchanged data, and present the results obtained from software injections of GW signals into the data and the related estimates of detection efficiencies and time errors for single detectors. Then we describe the coincidence analysis and background estimation for the network. The construction of confidence intervals on detected GWs is described in section 4. The results and final remarks are presented in sections 5 and 6, respectively. Finally, we report in appendix A a summary of the pipeline main steps and implementation, and in appendix B a complete calculation of the energy budget associated with the injected signals.

2. The search method

We present here an overview of the search method.

A specific search algorithm for each detector is run in order to produce lists of triggers. For each trigger the time and an estimate of the signal-to-noise ratio (SNR) are exchanged. For each detector, the exchanged lists comprise one derived by the analysis of the plain data from the detector and others obtained by adding to the data different MDC channels before running the event search algorithm. The thresholds used in this first step for each detector are chosen by the different collaborations in such a way that the triggers can be clearly identified and characterized.

2.1. Threshold optimization for coincident search

Generally, for a small increase in the threshold a large reduction of the background counts can be expected (see for example figure 6). The accidental coincidence rate between two detectors is proportional to the individual event rate, so we can act on one of the two thresholds or both. The tradeoff is the reduction of the detection efficiency. Sometimes the detected

magnitude of the injected events is large enough to allow increasing the threshold up to exclude any background coincidence, while in other time periods lower thresholds are preferred to preserve the detection efficiency.

In order to quantify these statements, we consider a gain function defined as the ratio between the number of detected events and the square root of the background count. The rationale for this choice derives from the procedure to set confidence intervals on the number of true coincidences. In fact, the background of accidental coincidences can always be subtracted from the found (total) number of coincidences. The residual of the subtraction is—loosely speaking—the number of truly correlated events between the detectors. In this sense, our gain function is the ratio between the average efficiency and the fluctuations of the background. We thus apply a time-varying threshold calculated for subsequent time segments by maximizing the gain function. This implies that for each time bin the threshold is set at the level corresponding to the maximum of the gain function for the pair of detectors. The overall result is that we apply over the entire data set and for each detector of the couple a non-constant cut on the event magnitude, using a variable threshold (the analysis pipeline is discussed in more detail in appendix A).

Figures 2 and 3 show two examples of such adaptive staircase thresholds. We choose as our source population damped sinusoid signals (DS) incoming from the galactic center (see section 3.1). The threshold was calculated every 30 min. In figure 2, DS with a central frequency of 914 Hz and a duration of 1 ms were injected. These wide frequency band signals are seen much better by Virgo than by AURIGA. Since all the events are coincident, the algorithm will clean up most of Virgo and AURIGA background events by raising, in this case, the threshold on Virgo and thus preserving the efficiency in AURIGA. A different situation is shown in figure 3: in this case, the injected signals are DS with a central frequency of 930 Hz and a duration of 30 ms. These are narrow band signals whose central frequency falls in a region of high sensitivity for AURIGA: the algorithm chooses mostly AURIGA as the more convenient detector for raising the threshold and eliminating coincident background events. For other combinations of detector couples and signal magnitudes the situation is different. In those cases, it is necessary to raise the threshold in both detectors to reach the desired value of the benchmark.

2.2. Background and efficiency of the network

The efficiency of detection is empirically defined by the sets of data containing MDC injections. The ratio between the coincident events due to injections found in the detector couple under study and the known number of injected events gives the empirical estimate of the efficiency. For the background estimation, we first take care of the (possible) true correlated events present in the data by shifting the times of the event lists of different detectors before looking for coincidences in time. By repeating this operation a number of times, we get renewed instances of the counting experiment: we will refer to this procedure as *time-delay analysis*. Altogether, the coincidences from hundreds of shifted configurations provide a rich population from which we can determine the main parameters of the background distribution.

The optimization procedure described in the previous section determines the cuts on the data set based on a function of the estimated background and efficiency. Hence these two estimates will be biased, sometimes severely, and cannot be used for setting confidence intervals. For this reason, we preliminarily divide the original data (accidental coincidences and MDC injections) into two equal size subsets. For the background we create two subsets by alternating shift index, while for the MDC we put the odd injections in the first subset and the even injections in the second subset. In both cases, one subset is used in the optimization

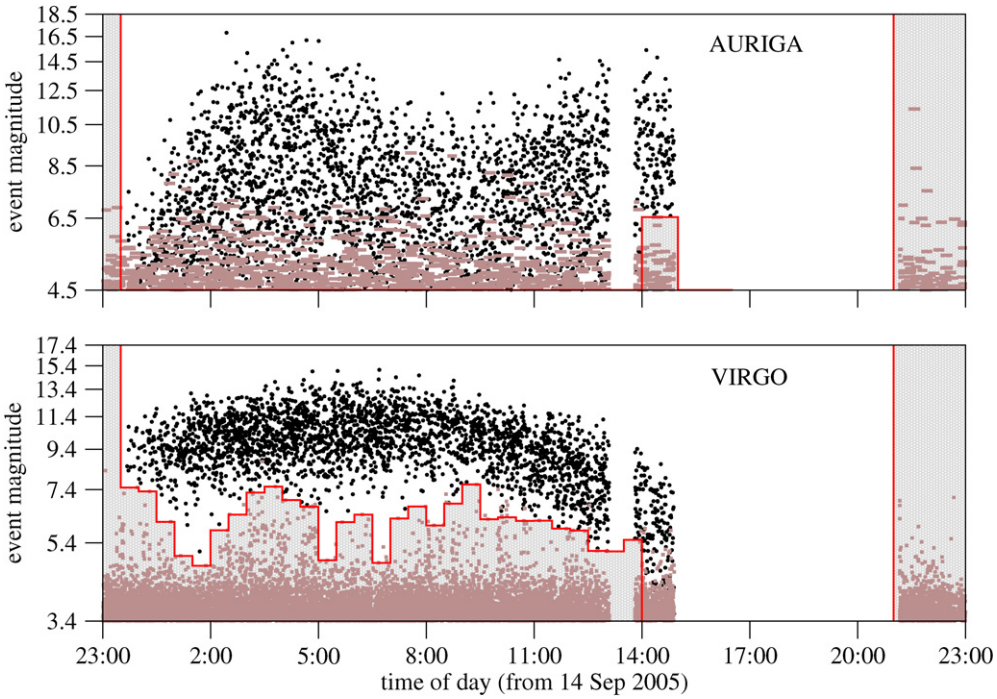

Figure 2. Example of threshold placing for detection optimization for the damped sinusoid DS (914 Hz; 1 ms) at $h_{\rm rss} = 10^{-19}$ Hz$^{-1/2}$ (see appendix B) for the couple AURIGA and Virgo. The abscissa represents the period of the exchanged 24 h of data taking, and the ordinate is the event magnitude given by the event trigger generators used by AURIGA and Virgo (see section 3.3). The light markers indicate background coincident events obtained by shifting the times of the event lists of the two detectors; the darker ones are events generated by injections. The modulation of the event magnitude by the antenna pattern is clearly visible in the two plots. The events form coincident couples, i.e. to each event in AURIGA the corresponding event in Virgo is plotted. Excluding one event from one detector automatically excludes the paired one in the other. Thus, given the relatively good separation of MDC events from background events in Virgo, the threshold here is raised up to the limit where basically all coincident background events are excluded, while the threshold in AURIGA is left almost at its initial value.

phase and the other in the estimation phase. The threshold levels obtained at the end of the optimization are subsequently applied to the second halves of the data, without further tuning. Background counts and efficiency are thus computed from this second subset, giving unbiased estimates.

3. The search implementation

In this section, we present the application of the search strategy described above to the Virgo-bars network search.

3.1. Target signals

The class of transient GW signals is extremely large; moreover, such signals may be generated by a large variety of astrophysical sources. In this scenario, we have chosen to constrain

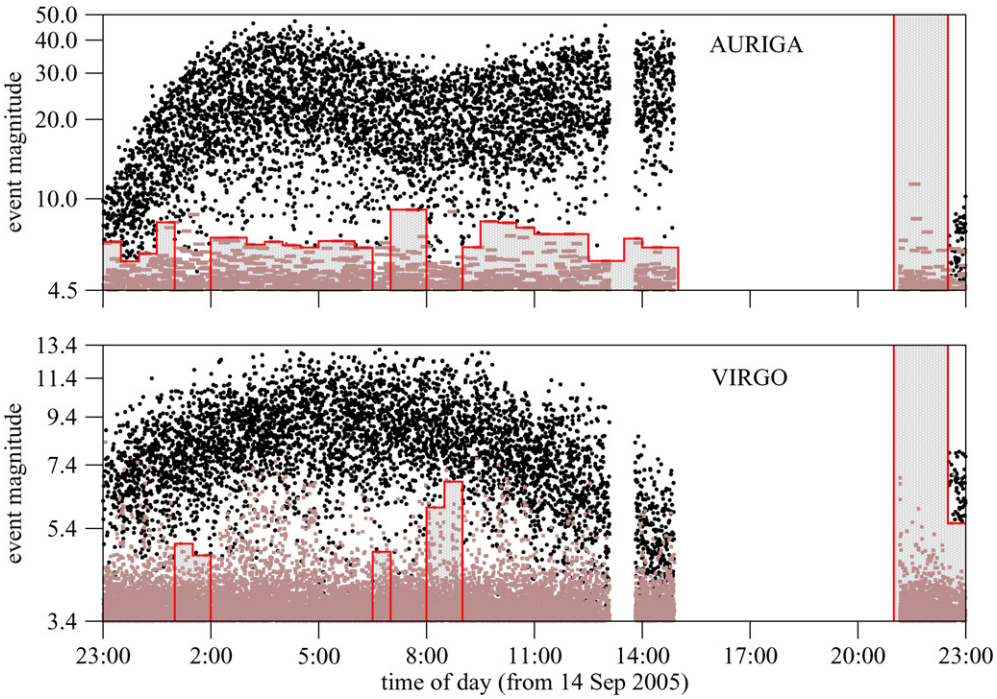

Figure 3. Example of threshold placing for detection optimization for the DS (930 Hz; 30 ms) at $h_{\rm rss} = 10^{-19}$ Hz$^{-1/2}$. In this case, the AURIGA threshold is raised almost everywhere in order to exclude coincident background triggers while preserving the efficiency of the network.

the source population to the ensemble of waveforms that can be analytically described as a damped sinusoid with the central frequency ranging within the bars bandwidths (850–950 Hz) and characterized by decaying times spanning at most a few tens of milliseconds. This choice is due to the different spectral densities of the various detectors in the collaboration (see figure 1), so that the interesting signals for our specific network are those whose power is concentrated in the bars most sensitive frequency range.

A typical damped sinusoid waveform is described by the following template:

$$u(t) = 0 \quad \text{for} \quad t < 0; \qquad u(t) \propto \mathrm{e}^{-t/\tau} \cos(2\pi f_0 t + \varphi_0) \quad \text{for} \quad t \geqslant 0 \tag{1}$$

where f_0 is the central frequency, τ is the damping time and φ_0 is the initial phase. These signals can be produced for instance by a ring-down phase following the merger of two black holes [17]. Other sources whose emission can be modeled by (1) are f-modes from neutron stars. The f-modes could produce a wave with variable frequency and damping time, which may sweep inside the observed frequency band [18]. To make a realistic detection, the energy release should be about 10^{-3}–$10^{-4} M_{\odot}$ for a galactic event (see appendix B.1).

The astrophysical model for our source population considers elliptically polarized signals (as sources angular momenta should have random directions with respect to the line of sight to the Earth) incoming from the galactic center.

3.2. Overview of exchanged data

The exchanged data consist of event lists corresponding to 24 h of data taking, starting from GPS time 810774700 or UTC time 14 Sep 2005 23:11:27. This choice corresponds to the longest stretches of continuous acquisition during the so-called C7 run of Virgo, when AURIGA, EXPLORER and NAUTILUS were in stable operation.

Each group exchanged the triggers found above a chosen threshold by their respective burst event search algorithms. No further tuning of parameters and amplitudes has been done at this stage.

Before exchanging all the data, the time information has been offset by a secret time shift within each group. This was done in order to prevent any bias which might arise by looking at the zero-delay coincidence counts in the tuning phase of the analysis.

It has to be noticed that the amplitudes may suffer from a systematic error due to the calibration uncertainty of each detector. This error is declared to be at most $\sim$30% for Virgo, $\sim$20% for EXPLORER and NAUTILUS, and $\sim$10% for AURIGA.

3.3. Event trigger generators

From the Virgo side, Power Filter [19] was the chosen event trigger generator. Power Filter searches on whitened data for a power excess using different time-analysis windows and different frequency bands and it uses as an indicator of the signal magnitude the SNR of the logarithm of the power. Events were exchanged at (logarithmic) SNR $\geqslant$ 3.4.

AURIGA group has successfully tested and implemented on its data WaveBurst event trigger generator, which is an excess power algorithm based on the wavelet transform developed by the LIGO Scientific Collaboration [20]; the exchange threshold was set at amplitude SNR $\geqslant$ 4.5. For the NAUTILUS and EXPLORER detectors the event trigger generator is an adaptive linear filter matched to the impulse response [21, 22]. The amplitude calibrated for the impulse response and the SNR were exchanged for each event and the exchange threshold was fixed at SNR $\geqslant$ 3.8.

3.4. Data quality: the correlograms

The correlograms, as shown in figure 4, are histograms of the time differences between the times of each possible couple of events. These allow us to investigate the level of auto-correlation of each detector and of correlation between two different detectors. For a Poisson point process one expects the histograms to be flat, i.e., without preferred time delays between events.

While single detectors, like Virgo, show some level of auto-correlation in the correlogram of the background events, on the other hand the cross-correlograms are flat as expected for random Poisson point processes. In the case of Virgo, in particular, the auto-correlogram presents a series of periodic ripples every about 2 s; this is the fundamental pendulum mode of the Virgo mirror suspension at a frequency of $\approx$0.6 Hz, whose excitation is only partially suppressed by the interferometer control loops. We found no evidence of modulation in the cross-correlation histograms up to $\pm$400 s. Moreover, we report in figure 4 the standard deviation for a pure Poisson process (horizontal straight lines). The data fluctuation is compatible with this hypothesis, except for Virgo auto-correlogram, because of the $\approx$0.6 Hz modulation.

Finally, we verified that no periodic correlation structure was present in the Fourier transform of any correlogram, except for the $\approx$0.6 Hz line of Virgo.

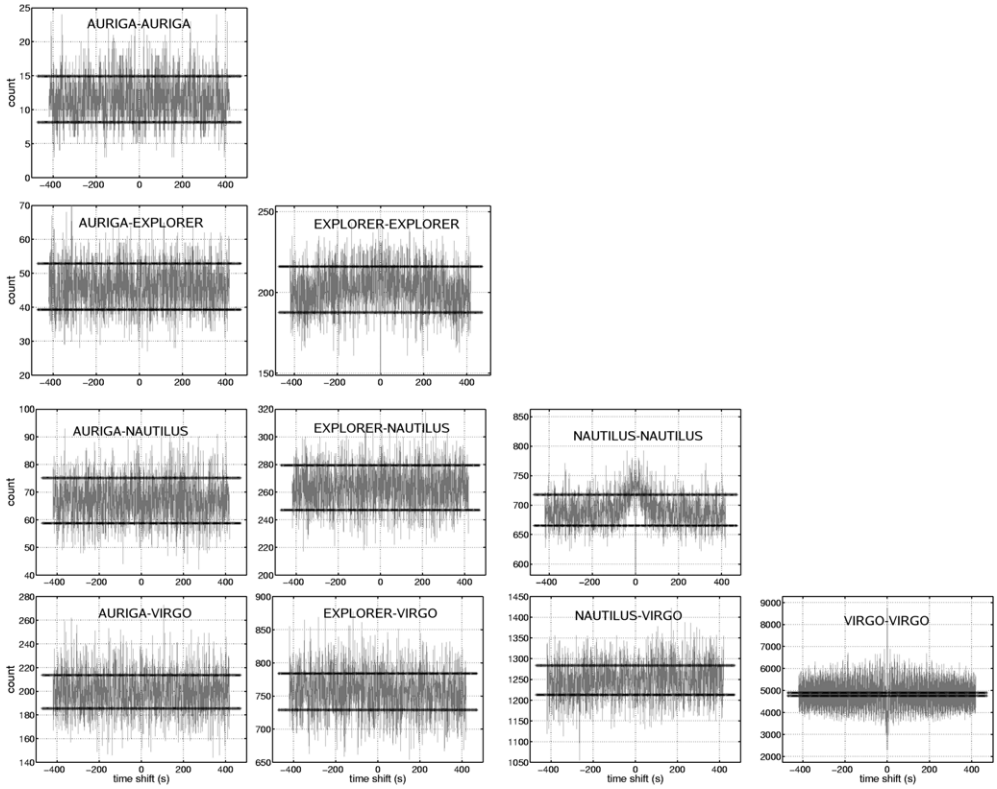

Figure 4. Correlograms and cross-correlograms for AURIGA, EXPLORER, NAUTILUS and Virgo. For each plot, the fluctuations are compared with the standard deviation from the mean calculated for a pure Poisson process. The NAUTILUS autocorrelogram show auto-correlation over a time scale of ± 100 s while the Virgo autocorrelogram shows periodic ripples every about 2 s. Anyway, the cross-correlograms are flat showing that there is no evidence of correlation between couple of detectors.

Table 1. The parameter space of DS signals is described by their central frequency f_0 and their decay time τ. The latter takes values spaced logarithmically by about a factor of 3, while the frequency axis is sampled at a special subset of frequencies, which was chosen on the basis of the typical narrow-band power spectral densities of the bars.

τ (ms)	f_0 (Hz)
1	914
3	882 946
10	866 898 930
30	866 874 906 930 938

3.5. Results from software injections

The injected GW signals consist of time series of sampled DS with f_0 within the sensitive frequency region for the resonant detectors, τ spanning between 1 and 30 ms (see table 1) and random elliptical polarization.

The source location is chosen at the galactic center. For each detector, a specialized time series is produced including the time delays and the amplitude attenuation due to the antenna

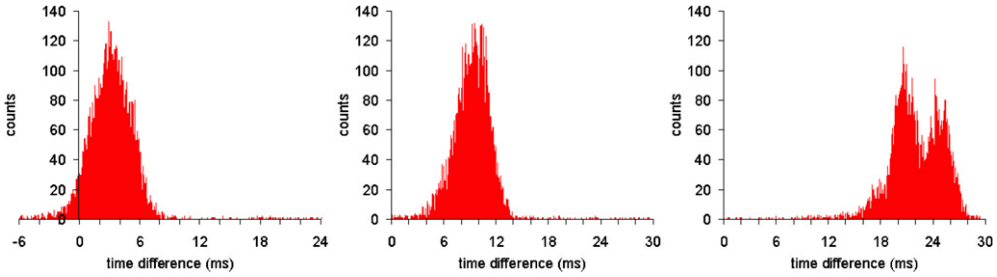

Figure 5. Distribution of time differences of detected events in coincident injection of DS (914 Hz; 1 ms) (left), DS (930 Hz; 10 ms) (center) and DS (930 Hz; 30 ms) (right), at $h_{\rm rss} = 10^{-18}$ Hz$^{-1/2}$ for the couple AURIGA-Virgo.

pattern (see for example the amplitude modulation in figure 2), using the SIESTA simulation software [23]. The simulated signals arrive at the Earth center approximately evenly spaced by 10 s (with a random jitter of ± 0.5 s), producing a set of 8640 injections over the 24 h observation time.

In the following, when referring to the 'amplitude' of the population, we mean the absolute $h_{\rm rss}$ amplitude of the wave, i.e. the amplitude at the Earth of the unprojected wave tensor (see appendix B.1). The generated waveform amplitudes for the coincidence analysis range between $h_{\rm rss} = 10^{-20}$ Hz$^{-1/2}$ and 10^{-18} Hz$^{-1/2}$ in order to span the curve of efficiency versus $h_{\rm rss}$ for all the detectors, see section 3.8.

We acknowledge a coarse approximation in the algorithm that calculates the samples amplitudes for the MDC, resulting in an overall underestimation of the injected signal strength $h_{\rm rss}$ with respect to the declared value. The effect of such an approximation is fully negligible for the most energetic signals, while it may cause a spurious loss of efficiency at the lowest amplitudes and for the less sensitive detectors. Nevertheless, the reported results are conservative and the methodological relevance of this work is not affected.

3.6. Time errors

The timing error of all search algorithms is heavily dominated by systematic biases. This is typical of algorithms that are not matched to the particular signal one is looking for. For instance, for the Virgo detector, the Power Filter's filter bandwidth is $\sim$100 Hz in the narrowest channel, and the time of arrival is determined by the time when the signal reaches its maximum amplitude. Because of this the biases for 1 ms and 10 ms long DS are 0.8 ms and 3.6 ms, respectively.

For the AURIGA detector, the bandwidth is narrower, causing a larger distortion of the signal. Moreover, the time associated with the event is computed as the baricenter of the signal profile above threshold. The amount of the bias depends strongly on the time duration and also on the central frequency of the signal. Altogether, for the durations $\leqslant$30 ms the bias for DS ranges from $\sim$3 ms to $\sim$30 ms depending on the central frequency [24].

The linear filter matched to a delta signal is unbiased for wide band signals, such as 1 ms long DS, but it is more biased as the signal duration gets longer [25]. For the considered DS the worst time error of EXPLORER and NAUTILUS was of the order of 8 ms and 16 ms for damping times $\tau = 10$ ms and $\tau = 30$ ms, respectively.

In figure 5 we see for example that the maximum time difference between AURIGA and Virgo is $\leqslant$30 ms.

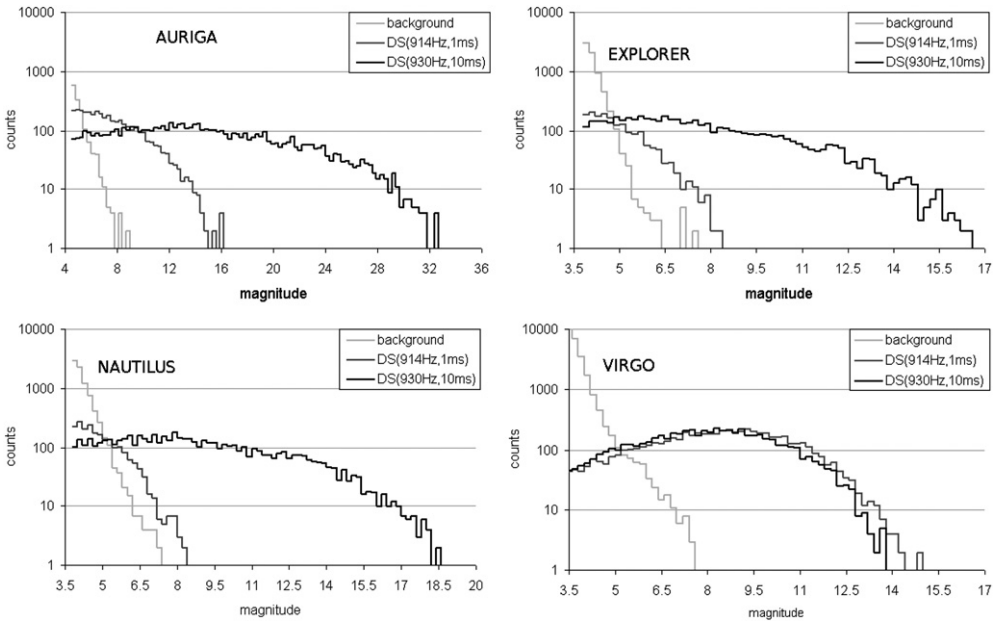

Figure 6. Distribution of detected 'event magnitudes' for background events and injections of DS (914 Hz; 1 ms) and DS (930 Hz; 10 ms) at $h_{\mathrm{rss}} = 10^{-19}\ \mathrm{Hz}^{-1/2}$ for AURIGA (top left), EXPLORER (top right), NAUTILUS (bottom left) and Virgo (bottom right). The 'magnitude' can be the SNR ratio given by WaveBurst algorithm (AU), the one given by a linear matched filter (EX and NA) and the logarithmic SNR of Power Filter (Virgo). Given the very different meaning of these quantities, the plots obtained for different detectors cannot be compared directly.

3.7. Distribution of amplitudes of accidental events and injected signals

The single detector search algorithms provide different estimates of the magnitude of the signal. Although not directly comparable among different detectors, the event magnitudes provided by each detector show how much the population of injected waveforms stems from the noise distribution. An example can be seen in figure 6.

3.8. Efficiency of detection

The software injections have also been used to monitor the detection efficiency of the single detectors. The efficiency is computed for different waveform amplitudes and using a ± 40 ms time window around the injection times: we look for coincidences between the injected signals and the events found by the event trigger generators. The calculation of the efficiency is based on the nominal 24 h allocated for this search. Consequently, dead times in the data due, for example, to epoch vetoes affect the average efficiency. This is the case for detector Virgo: its duty time is, in fact, far less than 100% in the 24 h considered (about 7 h are vetoed out because of bad data quality), which finally reduces the attainable average efficiency (see figure 7). The resonant detectors have instead a very stable duty cycle and they show improved performances with respect to Virgo when the signal is fully contained in their bandwidth (which requires special selection of the central frequency and long signal duration).

In conclusion, our definition of efficiency also includes dead times when data are missing or vetoed out from the nominal set, as we are interested in whether or not the network was able

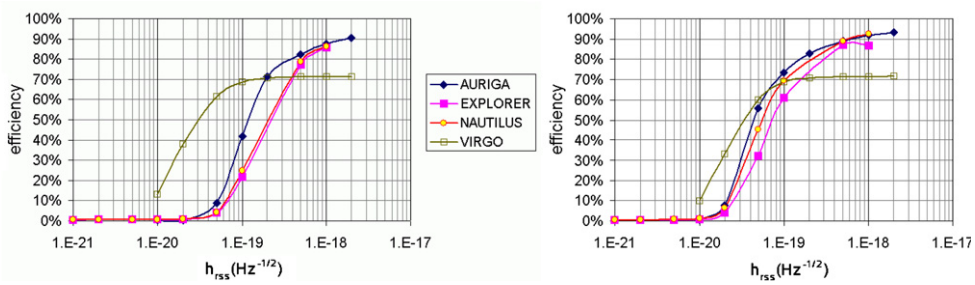

Figure 7. Efficiency of detection for the four detectors when recovering injections of DS (914 Hz; 1 ms) (left) and DS (930 Hz; 10 ms) (right) at different values of $h_{\rm rss}$. In the selected 24 h, ∼7 h of Virgo data have been excluded by epoch vetoes based on data quality. That is why efficiency levels at about 70%.

to recover the injected signals. We comply with this comprehensive definition of efficiency throughout the paper.

3.9. Coincidence analysis

A coincidence between two detectors is defined as the fulfilling of the relation

$$\left|t_{j_k}^{(k)} - t_{j_h}^{(h)} - \Delta t_{hk}\right| < T_w \tag{2}$$

where $t_{j_k}^{(k)}$ is the estimated time of arrival of the j_kth event in the detector labeled k and Δt_{hk} is the time of flight between the sites of the two detectors. For the case of our network and signals coming from the galactic center, the maximum time delay ranges between 0.3 ms for the couple Virgo–AURIGA and 2.4 ms for EXPLORER–NAUTILUS. From the results of the MDC injections (specifically, section 3.6), we set in the following $T_w = 40$ ms. After the tuning of the analysis, we checked, for all the configurations shown in table 2, that the loss in the overall efficiency with this coincidence time window is at most 1%.

3.10. Background estimation

As explained in section 2, we determine for each signal and each couple of detectors a time-varying threshold with time bins of 30 min. Eight hundred shifts are performed, half for threshold optimization and half for noise background estimation. Our time slides are spaced by 1 s and this guarantees that auto-correlation of detectors over a time scale equal to or less than 1 s is dissipated. In the case of Virgo and NAUTILUS, there is an auto-correlation over a larger time scale. Nonetheless, the cross correlograms show that the time-delay analysis decorrelates the couples of detectors (see figure 4).

If the time slide measurements are independent of each other, the number of accidental coincidences in each time shift should be Poisson distributed. We tested the hypothesis of Poisson distribution for the background by means of a χ^2 test just on those searches which have a high expected number of accidental coincidences so to ensure a sufficiently large data sample. The corresponding p-values were consistent with the Poisson model for the expected number of accidentals.

4. Setting confidence intervals

We set the confidence interval on the number of correlated events detected in coincidence following a unified approach in the spirit of [26]: we build a confidence belt to associate to any

Table 2. Results of the two-fold coincidence searches, for the chosen couples of detectors (see section 4.1) and for each set of the waveform parameters and amplitudes (second, third and fourth columns) for the exchanged 24 h data. The last four columns represent, respectively, the efficiency of detection measured by means of MDC injections, the average accidental coincidence counts (N_b), the number of coincidences found at zero delay (N_c) and the corresponding 95% upper limit. The errors associated with the efficiency and background estimates show the 1σ statistic fluctuation (*apices*).

Detector pair	f_0 (Hz)	τ (ms)	$h_{\rm rss}$ ($\rm Hz^{-1/2}$)	Efficiency (%)	N_b	N_c	UL counts ($\rm day^{-1}$)
AUR–VIR	914	1	5×10^{-20}	$5.1^{\pm 0.3}$	$0.046^{\pm 0.011}$	0	69.2
AUR–VIR	914	1	1×10^{-19}	$32.6^{\pm 0.7}$	$0.093^{\pm 0.016}$	0	10.9
AUR–VIR	914	1	2×10^{-19}	$54.0^{\pm 0.8}$	$0.101^{\pm 0.016}$	0	6.6
AUR–NAU	914	1	5×10^{-19}	$75.2^{\pm 0.7}$	$0.068^{\pm 0.014}$	0	4.7
AUR–NAU	914	1	1×10^{-18}	$83.0^{\pm 0.6}$	$0.071^{\pm 0.014}$	0	4.3
AUR–VIR	914	1	2×10^{-18}	$68.1^{\pm 0.7}$	$0.103^{\pm 0.017}$	0	5.2
AUR–VIR	882	3	5×10^{-20}	$16.3^{\pm 0.6}$	$0.086^{\pm 0.015}$	0	21.9
AUR–VIR	882	3	1×10^{-19}	$45.3^{\pm 0.8}$	$0.091^{\pm 0.016}$	0	7.8
AUR–VIR	882	3	2×10^{-19}	$58.5^{\pm 0.8}$	$0.098^{\pm 0.016}$	0	6.1
AUR–EXP	882	3	5×10^{-19}	$79.8^{\pm 0.6}$	$0.058^{\pm 0.012}$	0	4.5
AUR–EXP	882	3	1×10^{-18}	$86.6^{\pm 0.5}$	$0.056^{\pm 0.012}$	0	4.1
AUR–VIR	882	3	2×10^{-18}	$68.6^{\pm 0.7}$	$0.103^{\pm 0.017}$	0	5.2
AUR–VIR	946	3	5×10^{-20}	$16.2^{\pm 0.6}$	$0.091^{\pm 0.016}$	0	22.0
AUR–VIR	946	3	1×10^{-19}	$46.2^{\pm 0.8}$	$0.086^{\pm 0.015}$	0	7.7
AUR–VIR	946	3	2×10^{-19}	$58.6^{\pm 0.8}$	$0.088^{\pm 0.015}$	0	6.1
AUR–NAU	946	3	5×10^{-19}	$81.1^{\pm 0.6}$	$0.098^{\pm 0.016}$	0	4.4
EXP–NAU	946	3	1×10^{-18}	$85.9^{\pm 0.5}$	$0.036^{\pm 0.010}$	0	4.1
AUR–VIR	946	3	2×10^{-18}	$67.8^{\pm 0.7}$	$0.101^{\pm 0.016}$	0	5.2
AUR–VIR	866	10	5×10^{-20}	$21.0^{\pm 0.6}$	$0.078^{\pm 0.014}$	0	16.9
AUR–VIR	866	10	1×10^{-19}	$48.5^{\pm 0.8}$	$0.073^{\pm 0.014}$	0	7.3
AUR–VIR	866	10	2×10^{-19}	$60.2^{\pm 0.7}$	$0.063^{\pm 0.013}$	0	5.9
AUR–EXP	866	10	5×10^{-19}	$76.2^{\pm 0.6}$	$0.071^{\pm 0.014}$	0	4.7
AUR–EXP	866	10	1×10^{-18}	$84.3^{\pm 0.6}$	$0.053^{\pm 0.012}$	0	4.2
AUR–VIR	866	10	2×10^{-18}	$69.2^{\pm 0.7}$	$0.103^{\pm 0.017}$	0	5.1
AUR–VIR	898	10	5×10^{-20}	$22.3^{\pm 0.6}$	$0.083^{\pm 0.015}$	0	15.9
AUR–VIR	898	10	1×10^{-19}	$49.4^{\pm 0.8}$	$0.088^{\pm 0.015}$	0	7.2
AUR–VIR	898	10	2×10^{-19}	$60.4^{\pm 0.7}$	$0.088^{\pm 0.015}$	0	5.9
AUR–EXP	898	10	5×10^{-19}	$82.8^{\pm 0.6}$	$0.066^{\pm 0.013}$	0	4.3
AUR–EXP	898	10	1×10^{-18}	$87.7^{\pm 0.5}$	$0.068^{\pm 0.014}$	0	4.1
AUR–VIR	898	10	2×10^{-18}	$69.2^{\pm 0.7}$	$0.098^{\pm 0.016}$	0	5.1
AUR–VIR	930	10	2×10^{-20}	$2.4^{\pm 0.2}$	$4.1^{\pm 0.10}$	4	283.9
AUR–VIR	930	10	5×10^{-20}	$31.1^{\pm 0.7}$	$0.071^{\pm 0.014}$	0	11.4
AUR–NAU	930	10	1×10^{-19}	$61.9^{\pm 0.7}$	$0.068^{\pm 0.014}$	0	5.7
AUR–VIR	930	10	2×10^{-19}	$62.7^{\pm 0.7}$	$0.081^{\pm 0.015}$	0	5.7
EXP–NAU	930	10	5×10^{-19}	$83.7^{\pm 0.6}$	$0.036^{\pm 0.010}$	0	4.3
AUR–NAU	930	10	1×10^{-18}	$89.4^{\pm 0.5}$	$0.083^{\pm 0.015}$	0	4.0
AUR–VIR	930	10	2×10^{-18}	$69.3^{\pm 0.7}$	$0.103^{\pm 0.017}$	0	5.1
AUR–VIR	866	30	2×10^{-20}	$2.1^{\pm 0.2}$	$9.1^{\pm 0.15}$	11	508.1
AUR–VIR	866	30	5×10^{-20}	$25.5^{\pm 0.7}$	$0.021^{\pm 0.007}$	0	14.0
AUR–VIR	866	30	1×10^{-19}	$51.9^{\pm 0.8}$	$0.013^{\pm 0.006}$	0	6.8
AUR–VIR	866	30	2×10^{-19}	$61.8^{\pm 0.7}$	$0.053^{\pm 0.012}$	0	5.8
AUR–VIR	866	30	5×10^{-19}	$66.5^{\pm 0.7}$	$0.051^{\pm 0.012}$	0	5.3

Table 2. (Continued.)

Detector pair	f_0 (Hz)	τ (ms)	$h_{\rm rss}$ ($\rm Hz^{-1/2}$)	Efficiency (%)	N_b	N_c	UL counts ($\rm day^{-1}$)
AUR–EXP	866	30	1×10^{-18}	$78.8^{\pm 0.6}$	$0.068^{\pm 0.014}$	0	4.5
AUR–VIR	866	30	2×10^{-18}	$69.2^{\pm 0.7}$	$0.111^{\pm 0.017}$	0	5.1
AUR–VIR	874	30	2×10^{-20}	$2.4^{\pm 0.2}$	$9.5^{\pm 0.15}$	12	476.2
AUR–VIR	874	30	5×10^{-20}	$26.4^{\pm 0.7}$	$0.046^{\pm 0.011}$	0	13.5
AUR–VIR	874	30	1×10^{-19}	$51.5^{\pm 0.8}$	$0.033^{\pm 0.009}$	0	6.9
AUR–VIR	874	30	2×10^{-19}	$61.6^{\pm 0.7}$	$0.043^{\pm 0.011}$	0	5.8
AUR–EXP	874	30	5×10^{-19}	$73.1^{\pm 0.7}$	$0.076^{\pm 0.014}$	0	4.9
AUR–EXP	874	30	1×10^{-18}	$82.3^{\pm 0.6}$	$0.063^{\pm 0.013}$	0	4.3
AUR–VIR	874	30	2×10^{-18}	$69.8^{\pm 0.7}$	$0.111^{\pm 0.017}$	0	5.1
AUR–VIR	906	30	5×10^{-20}	$19.4^{\pm 0.6}$	$0.086^{\pm 0.015}$	0	18.4
AUR–EXP	906	30	1×10^{-19}	$48.0^{\pm 0.8}$	$0.061^{\pm 0.013}$	0	7.4
AUR–VIR	906	30	2×10^{-19}	$59.5^{\pm 0.7}$	$0.068^{\pm 0.014}$	0	6.0
AUR–EXP	906	30	5×10^{-19}	$82.8^{\pm 0.6}$	$0.066^{\pm 0.013}$	0	4.3
AUR–EXP	906	30	1×10^{-18}	$86.3^{\pm 0.5}$	$0.066^{\pm 0.013}$	0	4.1
AUR–VIR	906	30	2×10^{-18}	$69.3^{\pm 0.7}$	$0.103^{\pm 0.017}$	0	5.1
AUR–VIR	930	30	2×10^{-20}	$9.3^{\pm 0.4}$	$16.3^{\pm 0.20}$	16	116.2
AUR–NAU	930	30	5×10^{-20}	$45.4^{\pm 0.8}$	$0.043^{\pm 0.011}$	0	7.8
AUR–NAU	930	30	1×10^{-19}	$69.0^{\pm 0.7}$	$0.056^{\pm 0.012}$	0	5.2
AUR–VIR	930	30	2×10^{-19}	$64.0^{\pm 0.7}$	$0.023^{\pm 0.008}$	0	5.6
EXP–NAU	930	30	5×10^{-19}	$85.5^{\pm 0.5}$	$0.028^{\pm 0.009}$	0	4.2
AUR–NAU	930	30	1×10^{-18}	$90.0^{\pm 0.5}$	$0.081^{\pm 0.015}$	0	4.0
AUR–VIR	930	30	2×10^{-18}	$69.6^{\pm 0.7}$	$0.106^{\pm 0.017}$	0	5.1
AUR–NAU	938	30	2×10^{-20}	$4.6^{\pm 0.3}$	$3.0^{\pm 0.09}$	6	214.1
AUR–NAU	938	30	5×10^{-20}	$41.3^{\pm 0.7}$	$0.068^{\pm 0.014}$	0	8.6
AUR–NAU	938	30	1×10^{-19}	$68.1^{\pm 0.7}$	$0.078^{\pm 0.014}$	0	5.2
AUR–VIR	938	30	2×10^{-19}	$63.0^{\pm 0.7}$	$0.056^{\pm 0.012}$	0	5.6
AUR–NAU	938	30	5×10^{-19}	$86.9^{\pm 0.5}$	$0.081^{\pm 0.015}$	0	4.1
AUR–EXP	938	30	1×10^{-18}	$86.3^{\pm 0.5}$	$0.073^{\pm 0.014}$	0	4.1
AUR–VIR	938	30	2×10^{-18}	$70.2^{\pm 0.7}$	$0.098^{\pm 0.016}$	0	5.1

possible result of the experiment an interval which covers with a minimum chosen probability the true number of correlated events, whatever its value (zero or positive). The procedure we adopt to build the confidence belt derives from [27] and its fundamentals have been discussed in [7, 28]. As usual, in counting experiments, the noise model is Poisson and the likelihood of the number of coincidences at zero delay, N_c, as a function of the expected values of the accidental counts and of the correlated events, N_b and $N_{\rm GW}$ respectively, is

$$l(N_c; N_b, N_{\rm GW}) = \frac{(N_b + N_{\rm GW})^{N_c}}{N_c!}\, \mathrm{e}^{-(N_b+N_{\rm GW})}. \tag{3}$$

The confidence intervals on $N_{\rm GW}$ are then built by integrating the likelihood with respect to $N_{\rm GW}$,

$$I = \frac{\left[\int_{N_{\rm inf}}^{N_{\rm sup}} l(N_c; N_b, N_{\rm GW})\, \mathrm{d}N_{\rm GW}\right]}{\int_0^{\infty} l(N_c; N_b, N_{\rm GW})\, \mathrm{d}N_{\rm GW}} \tag{4}$$

to find the smallest interval $[N_{\rm inf}, N_{\rm sup}]$ corresponding to the chosen I value. The set of these intervals computed for the possible experimental results N_c gives the confidence belt

corresponding to a fixed level of background N_b. It is well known that the likelihood integral I cannot be interpreted as a frequentist probability. Therefore, the actual probability that the confidence intervals $[N_{\rm inf}, N_{\rm sup}]$ include the true $N_{\rm GW}$ value, i.e. the coverage of the confidence belt, must be empirically determined by a Monte Carlo [28]. This simulation is performed over a grid of many $N_{\rm GW}$ and N_b values in the interesting range, so to find the smallest I which can ensure a coverage greater or equal to the selected one. We choose to construct the confidence belt from the likelihood because this procedure offers nice features of the resulting confidence intervals, as for instance the fact that its upper limit when $N_c = 0$ is independent of the value of the background N_b (e.g. at 95% coverage, the upper limit is always 3.6 counts).

We modify the above confidence belt construction to increase the coverage in case no signals are present, $N_{\rm GW} = 0$, with respect to the minimum coverage for $N_{\rm GW} > 0$, as done in [16] for a different confidence belt construction. This is a useful feature, since the false claim probability of the experiment can get lower than 1 minus the minimum coverage of the confidence belt: in the following we set a false claim probability of 1% with a confidence belt of 95% minimum coverage. The required modification affects the lower bound of the belt, which is extended down to zero for the N_c values that pass the null hypothesis test with 99% significance. In our case, the null hypothesis test is a Poisson one-tail test on N_c assuming $N_{\rm GW} = 0$, i.e. no correlated signals. As a result, the lower bound of the confidence intervals detaches from zero at higher N_c, where the null hypothesis is rejected. As long as this modification is decided *a priori* and it becomes part of the procedure of the confidence belt construction, its effects are compliant with the unified approach. The price to pay is an additional overcoverage for the lower range of $N_{\rm GW}$ values.

4.1. Multiple trials and global confidence

In this analysis, we perform about 400 searches for different signal waveforms and amplitudes by different detector pairs, i.e. our search has a large *trial factor*. This, of course, affects the probability of false claim of the whole experiment. In the simplified case of an experiment involving N_t independent trials, the global probability of false claim is given by

$$p = 1 - (1 - p_0)^{N_t}$$

where p_0 is the false claim probability on the single trial.

Since in our experiment the trials are partially correlated, we measure the global probability of false claim using independent resamplings of the coincidence experiment where no correlated events are present. These resamplings are obtained by time shifting the original data sets so that the resulting coincidences are accidental. A set of 400 resamplings has been used to empirically estimate the distribution of the accidental coincidences and to measure the relation between the global confidence of detection of the whole experiment, $1 - p$, and the nominal confidence of the null hypothesis test on each trial, $(1 - p_0)$, see figure 8. In particular, setting a single trial confidence $1 - p_0 \sim 0.999$ results in a global confidence $1 - p \geqslant 95\%$.

We require a lower target false claim probability for the whole experiment: $p \leqslant 1\%$. To achieve this reduction, we decrease the trial factor of the experiment instead of increasing the confidence of the null hypothesis test on each trial. In fact, since the accidental background of single trials is typically $N_b \sim 0.1$, 0.999 confidence requires at least three coincidences in a single trial to reject the null and make a claim for correlated events: this threshold of 3 counts is already quite higher than the expectations for correlated events in the participating detectors and therefore we have to rule out further increases of $1 - p_0$.

The reduction of the trial factor is accomplished by selecting only one configuration of detectors for each target waveform and amplitude, leaving a subset of 72 searches. The

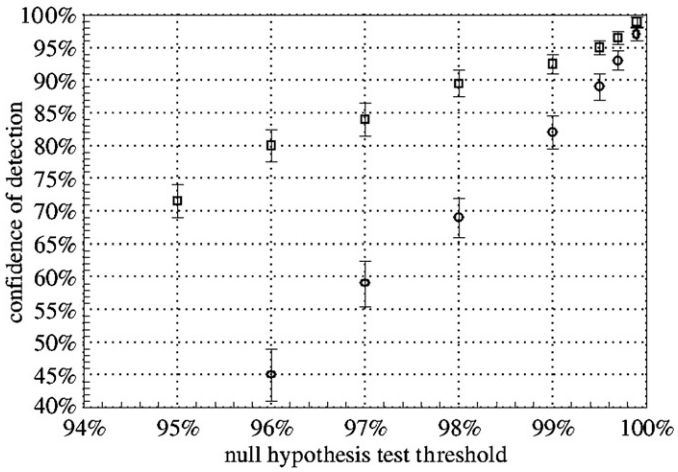

Figure 8. Measured global confidence of detection over all configurations versus nominal confidence of the null hypothesis test for each single search. The circles refer to the full list of trials (about 400), and the squares to the subset of the 72 selected detector configurations capable of setting the best upper limits for each waveform and wave amplitude.

selection is performed by looking for the pair of detectors which are performing best, i.e. capable to set the most stringent upper limit (square data points in figure 8). More specifically, we compute fake upper limits for each trial by taking the mean value of the upper limits computed for each shift, using for N_c the number of background coincidences in that shift. Hence, for each waveform and amplitude, we select the detector pair producing the lowest fake upper limit. Only the selected subset of configurations are then used to draw the final results of the search, by looking at their true coincidences N_c. In this way, the trial factor is significantly reduced and the same significance on the null hypothesis test for each single trial, $1 - p_0 = 0.999$, produces the target false claim probability, $p < 1\%$.

5. Results

As a last step, we searched for coincidences at the true time in all the selected configurations. The final outcome was consistent with the null hypothesis test at 99.9% confidence for each configuration, corresponding to a global false claim probability of 1%. The confidence intervals are, therefore, upper limits on the rate of incoming GWs.

Detailed results are presented in table 2, where, for each injected waveform, the estimated efficiency, the average background, the zero-lag coincidence counts and the corresponding 95% upper limit are reported. We also included a few configurations with low amplitude signals: in order to preserve the residual efficiencies, the related average backgrounds are quite high, leading to non-null zero-delay coincidence counts.

Figure 9 shows the upper limits as a function of the signal amplitude. The asymptote for large amplitude signals is inversely proportional to the observation time and the asymptotical efficiency and depends on the confidence belt: for this 24 h search, it is $\simeq$4.0 events/day, as our maximum efficiency is $\simeq$90% and the chosen confidence belt (see section 4) with 95% CL sets a pretty conservative value (3.6 counts).

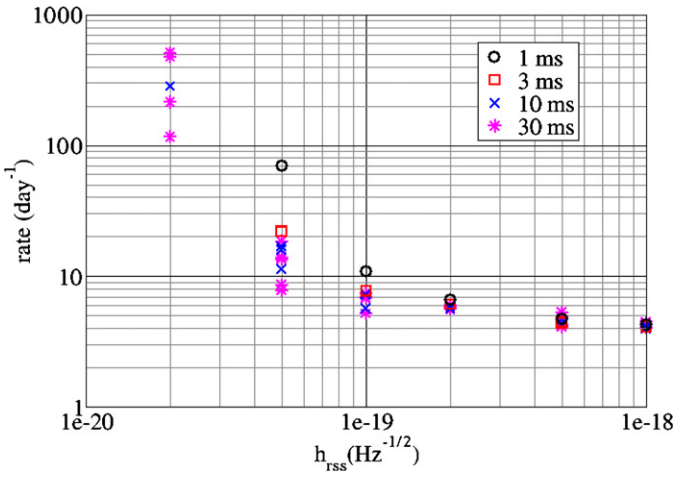

Figure 9. Upper limit at 95% conservative coverage on the event rate as a function of the population amplitude for the exchanged 24 h data. Upper limits referring to the same duration of the signal but different central frequencies are grouped with the same symbol. Note that the systematic error of about 10–30% on the amplitude calibration has not been taken into account.

6. Final remarks

We presented a methodological study for analyzing data collected by a network of non-homogeneous detectors. The search was aimed at detecting transient GW signals. We implemented a two-fold time coincidence search; however, this method can be applied to any detectors combination as well, e.g. three-fold, logical 'OR' of two-fold, etc. For each set of waveform parameters and amplitudes, six different couples of detectors were available: we chose to perform our search on those couples which allow potentially the set up of the most stringent upper limit (see section 4.1).

The key point of the method is the optimization process of the analysis thresholds for a given source population by means of Monte Carlo MDC injections.

Although the proposed methodology is viable for any specific signal model, including the sky distribution of the sources, in the present study we assumed DS signals incoming from the galactic center, limiting our observation range to our galaxy.

Moreover, in order to estimate the detection efficiency of the network we applied a standard Monte Carlo procedure based on a large set of injected signals. Although this software technique is computationally intensive, it permits us to derive reliable values of the efficiency and unbiased physical interpretation of the results, i.e. the GW amplitudes and rates of the population under study. The injections were actively used in the search phase, i.e. not only for the interpretation of results but also for the optimization of the exclusion thresholds. However, we point out a limitation of this procedure: each separate optimization targeting to a different source produces a partially statistically independent result. As a consequence, the large final trial factor imposes the modification of the confidence belt at low counts in order to keep the accidental detection probability under control. This limits the detection power at low signal counts.

Finally, we note that in the procedure presented here the statistical test relies just on the event magnitude. However, we stress that it is possible to extend the method either by

including other statistical tests in the definition of the local event trigger generators or by implementing a common maximum likelihood estimator (χ^2 test).

Acknowledgments

We acknowledge the funding from EU FP6 Programme-ILIAS. Lucio Baggio was supported by the EGO Consortium. Virginia Re was supported by EGO-VESF Fellowship, call 2005.

Appendix A. Optimization pipeline

We present here a schematic overview of all the steps:

A.1. Coincidence search

- For each couple of detectors, the plain data sets are searched for coincidences after adding 800 offsets in steps of 1 s, with a time window of 40 ms. This covers about 7 min before and after the unshifted time, with a safety range of ± 20 s around the zero-delay time[44].
- All the lists with MDC injections are searched for coincident events (obviously no time-delay analysis is performed in these cases) and the detection efficiency is thus evaluated.

A.2. Optimization procedure

- The data are split into two equal sets, one used in the optimization phase, and the other in the estimation phase. For the MDC injections we follow the chronological order by putting odd and even injections alternatively in the first or the second subset. In the case of the coincidence background we alternate on shift index.
- The data are divided in 30 min long time bins.
- We evolve a couple of staircase thresholds (jointly for the two detectors) by increasing the threshold level in one time bin and one detector at a time. At each step, in order to have a significant variation, the test threshold is increased by an amount which corresponds to a reduction in the background counts of the order of the standard deviation of the counts themselves[45]. Moreover, when a time bin is found to give a small contribution ($<0.1\%$) to the efficiency, we eliminate it by raising the threshold in that bin up to the level where all the background events are cut off.
- At the nth step of the algorithm, we compute the ratio $N_{\mathrm{eff}}^{(n)}/\sqrt{N_b^{(n)}}$, where $N_{\mathrm{eff}}^{(n)}$ and $N_b^{(n)}$ are the *total* number of MDC coincidences and background coincidences from the set reserved for the optimization whose associated amplitudes are above the nth set of thresholds. Then the effect of increasing the threshold of one level at one bin is evaluated by computing the new ratio $N_{\mathrm{eff}}^{(n+1)}/\sqrt{N_b^{(n+1)}}$. Every time the bins in both detectors are tried one by one in order to find for which a threshold change would score the higher benchmark. If this benchmark is better than that obtained at the previous step, the level for that bin is changed, and this is taken as the starting point for the next loop. Instead, if all changes resulted in a decrease of the benchmark, the loop is exited. The loop will otherwise continue up to reaching the higher level of thresholds.

[44] We recall that 10 s is the maximum value for the blind shift applied previously to data exchange, see section 3.2.
[45] We found empirically that the square root of the counts divided by 6 is a good compromise. Yet, we impose that the background decrease is of at least 4 counts.

- At the end of the loop, we refine the found optimized thresholds in case the algorithm got stuck at a false maximum. To this purpose, for each bin we recompute the benchmark $N_{\rm eff}/\sqrt{N_b}$ without that bin and we evaluate whether it is convenient to keep it or whether removing it would be an improvement.
- The found set of thresholds are applied to the alternative sets of triggers which were kept aside in order to re-estimate unbiased values for $N_{\rm eff}$ and N_b. These two numbers, divided respectively by the number of injected events (4320) and of time-shifted configurations (400), give the estimates for the efficiency of detection and for the average background counts.

A.3. Efficiency and confidence

- For each shifted configuration of the alternative set, $N_{\rm eff}$ and N_b are used to compute the corresponding upper limit at 95% confidence.
- This entire procedure is repeated for a different couple of detectors and/or a different set of MDC injections.
- After having decided the level of confidence for the eventual rejection of the null hypothesis, we unveil the coincidence counts at zero delay and compute for them confidence interval.

Appendix B. Details about the injected signals

In this study we assume that the waveforms, in the TT gauge, are of the form

$$\begin{pmatrix} h_+ \\ h_\times \end{pmatrix} = \frac{h_{\rm rss}}{\pi f_{\rm gw}\tau}\sqrt{\frac{1+4\pi^2 f_{\rm gw}^2\tau^2}{\tau(1+{\rm e}^{-1/(2f_{\rm gw}\tau)})}}\,{\rm e}^{-t/\tau}\begin{pmatrix} \cos 2\psi & -\sin 2\psi \\ \sin 2\psi & \cos 2\psi \end{pmatrix} \times \begin{pmatrix} \frac{1+\cos^2\iota}{2}\Theta\left(t-\frac{1}{4f_{\rm gw}}\right)\cos(2\pi f_{\rm gw}t) \\ \cos\iota\,\Theta(t)\sin(2\pi f_{\rm gw}t) \end{pmatrix} \tag{B.1}$$

where the angle ψ is an arbitrary polarization and the angle ι is an arbitrary inclination of the angular momentum of the system which originates the burst with respect to the line of sight.

Note the different Θ for the h_+ and $h_\times$ terms; the reason for multiplying $\cos(2\pi f_{\rm gw}t)$ by $\Theta\left(1-\frac{1}{4f_{\rm gw}}\right)$ is to avoid a discontinuity at the beginning of the waveform, which would result into an infinite energy, even though $h_{\rm rss}$ would remain finite.

The polarization ψ is uniformly distributed in $[0, 2\pi)$, while $\cos i$ is uniformly distributed in $[-1, 1)$; these choices correspond to assume a random orientation in space of the axis of symmetry of the emitting system.

B.1. Signal normalization

The signal normalization is done requiring equation (B.2) for $\psi = 0, \iota = 0$:

$$h_{\rm rss}^2 \equiv \int_0^\infty (|h_+(t)|^2 + |h_\times(t)|^2)\,{\rm d}t. \tag{B.2}$$

It can also be useful to relate $h_{\rm rss}$ and the energy emitted E assuming a source located at a distance r. To this end, we recall the standard definition of the energy flux

$$\frac{{\rm d}E}{{\rm d}A\,{\rm d}f} = \frac{\pi c^3}{2G_N} f^2(|\tilde{h}_+(f)|^2 + |\tilde{h}_\times(f)|^2) \tag{B.3}$$

where $dA = r^2\,d\Omega$. It is straightforward to compute

$$(|\tilde{h}_+(f)|^2 + |\tilde{h}_\times(f)|^2) = h_{\rm rss}^2 \frac{\tau\left(4f_{\rm gw}^2\pi^2\tau^2+1\right)}{\left(1+e^{\frac{1}{2f_{\rm gw}\tau}}\right)} \times \frac{\left(\cos^4(i)+\left(2+4\,e^{\frac{1}{2f_{\rm gw}\tau}}\right)\cos^2(i)+1\right)}{\left(16f^4\pi^4\tau^4+\left(4f_{\rm gw}^2\pi^2\tau^2+1\right)^2+f^2\left(8\pi^2\tau^2-32f_{\rm gw}^2\pi^4\tau^4\right)\right)} \tag{B.4}$$

and then, after performing the integral over frequencies and the angles, one obtains

$$E = \frac{\pi c^3 r^2 h_{\rm rss}^2\left(4f_{\rm gw}^2\pi^2\tau^2+1\right)}{2G_N}\frac{\left(7+5\,e^{\frac{1}{2f_{\rm gw}\tau}}\right)}{30\left(1+e^{\frac{1}{2f_{\rm gw}\tau}}\right)\pi\tau^2}, \tag{B.5}$$

i.e.,

$$\frac{E}{M_\odot c^2} \simeq 10^{-6}\frac{\left(1+(5/7)\,e^{\frac{1}{2f_{\rm gw}\tau}}\right)}{\left(1+e^{\frac{1}{2f_{\rm gw}\tau}}\right)}\left(1+\frac{1}{4\pi^2\tau^2 f_{\rm gw}^2}\right)\left[\frac{h_{\rm rss}}{10^{-21}/\sqrt{\rm Hz}}\right]^2\left[\frac{r}{10\ {\rm kpc}}\right]^2\left[\frac{f_{\rm gw}}{1\ {\rm kHz}}\right]^2 \tag{B.6}$$

which means that observing an $h_{\rm rss} \simeq 10^{-21}\ {\rm Hz}^{-1/2}$ with signals at about 1 kHz corresponds to a source emitting a fraction $\sim 10^{-6}$ of a solar mass in gravitational waves at a distance of 10 kpc.

References

[1] Baggio L *et al* 2005 *Phys. Rev. Lett.* **94** 241101
[2] Vinante A (for the AURIGA Collaboration) 2006 *Class. Quantum Grav.* **23** S103
[3] Astone P (for the ROG Collaboration) 2004 *Class. Quantum Grav.* **21** S1585
[4] Astone P *et al* 2006 *Class. Quantum Grav.* **23** S57
[5] Acernese F (for the Virgo Collaboration) 2006 *Class. Quantum Grav.* **23** S635, and references therein
[6] Allen B Z (for the IGEC Collaboration) 2000 *Phys. Rev. Lett.* **85** 5046
[7] Astone P *et al* (IGEC Collaboration) 2003 *Phys. Rev.* D **68** 022001
[8] Amaldi E *et al* 1989 *Astron. Astrophys.* **216** 325
[9] Astone P *et al* 2002 *Class. Quantum Grav.* **19** 5449
[10] Astone P *et al* 2006 *Class. Quantum Grav.* **23** S169
[11] Abbott B *et al* (LIGO Scientific Collaboration) 2004 *Phys. Rev.* D **69** 102001
[12] Abbott B *et al* (LIGO Scientific Collaboration) 2005 *Phys. Rev.* D **72** 062001
[13] Abbott B *et al* (LIGO Scientific Collaboration) 2006 *Class. Quantum Grav.* **23** S653
[14] Abbott B *et al* (LIGO Scientific Collaboration) 2005 *Phys. Rev.* D **72** 122004
[15] Cadonati L *et al* 2005 *Class. Quantum Grav.* **22** S1337
[16] Baggio L *et al* 2008 *Class. Quantum Grav.* **25** 095004
[17] Kokkotas K D and Schmidt B G 1999 *Living Rev. Rel.* **2** 2 (http://www.livingreviews.org/lrr-1999-2)
[18] Ferrari V *et al* 2003 *Mon. Not. R. Astron. Soc.* **342** 629
[19] Guidi G M, Cuoco E and Viceré A 2004 *Class. Quantum Grav.* **21** S815
[20] Klimenko S *et al Waveburst Version 5* LIGO-T050222-00-Z
[21] Astone P *et al* 1997 *Nuovo Cimento* **20** 9
[22] D'Antonio S 2002 *Class. Quantum Grav.* **19** 1499
[23] Caron B, Flaminio R, Marion F, Mours B, Verkindt D, Cavalier F and Viceré A 1999 *Astropart. Phys.* **10** 369
[24] Drago M 2006 Private communication
[25] Astone P, D'Antonio S and Pai A 2006 *J. Phys.: Conf. Ser.* **32** 192
[26] Feldman G J and Cousins R D 1998 *Phys. Rev.* D **57** 3873
[27] Roe P B and Woodroofe M B 2000 *Phys. Rev.* D **63** 090013
[28] Baggio L and Prodi G A 2003 *Proc. Conf. on Statistical Problems in Particle Physics, Astrophysics and Cosmology (PHYSTAT 2003) (Menlo Park, CA, 8–11 Sept. 2003)* ed R Mount, L Lyons and R Reitmeyer (Stanford, CA: SLAC) p 238 (http://www.slac.stanford.edu/econf/C030908/papers/WELT003.pdf) (*Preprint* astro-ph/0312353)